

Relevance of the Formation of Intermediate Non-Equilibrium Phases in $\text{YBa}_2\text{Cu}_3\text{O}_{7-x}$ Film Growth by Transient Liquid-Assisted Growth

Silvia Rasi,* Laia Soler, Julia Jareño, Juri Banchewski, Roger Guzman, Cristian Mocuta, Martin Kreuzer, Susagna Ricart, Pere Roura-Grabulosa, Jordi Farjas, Xavier Obradors, and Teresa Puig

Cite This: *J. Phys. Chem. C* 2020, 124, 15574–15584

Read Online

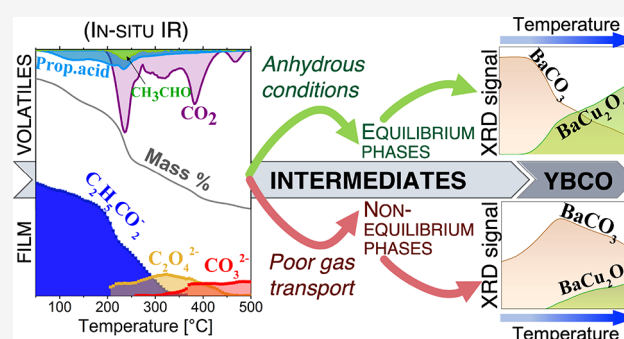
ACCESS |

Metrics & More

Article Recommendations

Supporting Information

ABSTRACT: Transient liquid-assisted growth (TLAG) is a non-equilibrium ultrafast method to grow $\text{YBa}_2\text{Cu}_3\text{O}_{7-x}$ (YBCO) superconducting films at up to 100 nm/s using chemical solution deposition. In this work, we study the formation of non-equilibrium crystalline intermediate phases prior to the growth of YBCO through TLAG. We analyze the thermal decomposition and microstructural evolution of a propionate-based fluorine-free solution used as precursor to YBCO epitaxial films. Thermal analyses (TGA, DSC), coupled with techniques to monitor the volatiles (TG-IR), were applied in situ during film pyrolysis in humid O_2 , while the thermal evolution of the solid residue was characterized by infrared spectroscopy and X-ray diffraction, both ex situ and in situ in synchrotron radiation sources, and by scanning transmission electron microscopy (STEM) and electron energy loss spectroscopy (EELS) cross-sectional analysis. Unexpected effects, observed during the decomposition of the ternary solution, are the formation of intermediate non-equilibrium phases: Cu_2O or $\text{Cu}(0)$ and monoclinic BaCO_3 . We emphasize that working with anhydrous solutions and anhydrous deposition conditions promotes the formation of the expected equilibrium phases. Finally, in situ X-ray diffraction permits monitoring the influence of the non-equilibrium monoclinic BaCO_3 phase on the formation of binary oxide phases, precursors of TLAG YBCO film growth. Understanding the evolution of non-equilibrium phases is shown to be fundamental for the control of the final YBCO film's microstructure and performance, since the latter are strongly affected by the film's thermal history after solution deposition.



INTRODUCTION

$\text{YBa}_2\text{Cu}_3\text{O}_{7-x}$ (YBCO) is a rare-earth (RE) oxide used to fabricate second-generation high-temperature superconducting (HTS) tapes,^{1–4} which find applications in the fields of energy transport and electrical power devices, among others.⁵ One of the greatest challenges that still limits their applications is the strong need for cost-effective fabrication methodologies. For these reasons, chemical methods like chemical solution deposition (CSD)^{5,6} have arisen as a low-cost alternative. Optimization of CSD methods relies on the understanding of the processes involved in the thermal treatments that the precursor solution undergoes after deposition. Of particular importance is the low-temperature stage of pyrolysis, where many physical and chemical transformations take place as a consequence of the organic material removed.

Recently, we have developed a non-equilibrium growth process that combines CSD with the ultrafast growth from transient liquids, the so-called transient liquid-assisted growth through CSD (TLAG-CSD),⁷ which can obtain YBCO epitaxial films with YBCO growth rates 100-times faster than the well-known fluorinated precursor route.^{2,3,8–11} In this regard, the interest of this work lies in analyzing the fluorine-

free (FF) solutions¹² used in TLAG-CSD. Additionally, FF precursors are more environmentally friendly than fluorinated precursors, because they do not generate hydrofluoric acid as a decomposition product. In particular, FF solutions based on acetate salts dissolved in excess propionic acid^{13–15} have gained attention. In these solutions, exchange of acetate groups for propionates takes place, with formation of the corresponding propionate salts.

With the aim of understanding the processes involved during the pyrolysis and heating stages, thermal analysis (TA) techniques coupled to spectroscopic and microstructural studies are a fundamental tool; however, many studies concerning the thermal decomposition of metalorganic precursors such as metal carboxylates^{16–20} deal with samples in the form of powders, because the signal-to-noise ratio in TA

Received: April 30, 2020

Revised: June 11, 2020

Published: June 16, 2020



is significantly reduced for samples in the form of film. The possibility of applying TA to films, despite the much smaller amount of material, has led to the knowledge that powders behave differently than films^{21,22} due to slower heat dissipation²³ and gas transport. Following this new interest in the TA of films, and for metal propionates in particular, it was found that the thermal behavior is strongly influenced by the nature of the metal cation.²⁴ Those metals that easily undergo reduction (Cu, Ag, and Hg) tend to break on the M–OC=O bond,^{25–27} while for the other class of metals (Ca, Ba, Y, etc.) the preferable cleavage site is the MO–C=O and MOC(=O)–C bond.^{18,28–30} According to this behavior, in humid O₂, copper propionate (Cu(C₂H₃CO₂)₂, abbreviated as CuProp₂) was found to decompose releasing propionic acid through the hydrolysis path to form CuO.³¹ Conversely, barium propionate (shortened as BaProp₂) in humid O₂ releases mainly acetaldehyde and CO₂ via the oxidation path.³² No propionic acid is observed given the fact that an oxalate (BaC₂O₄) is the decomposition intermediate, which retains both –CO₂ groups of the propionate units, impeding decomposition through the hydrolysis path. Finally, yttrium propionate (YProp₃) in humid O₂ exhibits both mechanisms,³³ releasing propionic acid via hydrolysis and acetaldehyde and CO₂ to yield an oxycarbonate (Y₂O₂CO₃) before this decomposes to the oxide, yttria (Y₂O₃).

We are interested in humid atmospheres, since they can favor decomposition at low temperatures through the hydrolysis path. This low-temperature mechanism favors CuProp₂ more than the other two salts, because it decomposes at sufficiently low temperatures, between 100 and 200 °C in films. It is followed by YProp₃, between 200 and 400 °C, and finally BaProp₂, between 250 and 500 °C. Although the single components have been fully characterized, a study of the thermal behavior of this ternary solution is needed to confirm whether the behavior of a ternary mixture can be straightforwardly extrapolated from its components.

In this work we report on TA in humid O₂ of a propionate-based FF ternary solution by comparing its behavior with that of its binary and single-salt solutions. To characterize the thermal behavior, thermogravimetric analysis (TGA) is coupled with evolved gas analysis (EGA) via infrared detection (TG-IR) of the gas species evolved during decomposition. Solid intermediates and products are characterized by X-ray diffraction (XRD) and Fourier transform infrared spectroscopy (FTIR), both ex situ and in situ using synchrotron sources. Results show that the thermal behavior of the ternary mixture differs from that expected from the simple sum of its components (i.e., the single-salt solutions) in terms of products and crystalline phases formed. We show the undesirable effects of water content in solutions in terms of microstructure and crystalline phases formed. In particular, water is connected with the formation of a non-thermodynamically stable phase of BaCO₃, the monoclinic phase. Finally, some comments on how to avoid these non-equilibrium phases are presented within the framework of cost-effective CSD methodologies.

METHODS

Materials and Film Preparation. A propionate-based metal–organic solution was prepared starting from yttrium acetate (Y(CH₃CO₂)₃, YAc₃, Alfa Aesar, 99.99%), barium acetate (Ba(CH₃CO₂)₂, BaAc₂, Sigma-Aldrich, 99.99%), and copper acetate (Cu(CH₃CO₂)₂, CuAc₂, Alfa Aesar, 99.99%) and dried at 55 °C in a thermostatic vacuum dryer (Vaciotem-

T, from Selecta). Then they were dissolved in propionic acid (Merck, ≥99%). After complete dissolution of the salts, methanol (MeOH, VWR, ≥99.8%) was added to reach a 1/1 ratio of solvents with total metal content of 1 M. The ternary solution was prepared with a molar ratio of Y/Ba/Cu = 1/2/3. Binary solutions of all three precursors were also prepared for comparison, based on the same metal ratios and labeled as Cu–Ba, Y–Ba, and Cu–Y. In all these solutions, due to excess propionic acid, replacement of acetates by propionates is expected to take place to yield the corresponding propionate salts after drying. For the barium salt, the replacement is only partial, yielding a mixed propionate–acetate complex.^{32,34}

Films were prepared by depositing the solutions on LaAlO₃ (LAO) substrates of 1 × 1 cm² in lateral size, which were then dried at 80 °C for 2 min on a hot plate. For thin films (<1 μm of YBCO), deposition was realized through spin-coating; thick films (≥1 μm) were prepared by drop-casting. The (approximate) nominal final thickness, *h*, of the film was calculated knowing the final oxides and carbonate density (ρ), and the surface area (*A*) using the following formula: $h = m/(\rho \times A)$. The anhydrous ternary solution was prepared in the same way but using anhydrous methanol (Scharlau, 99.9%); it was kept in a sealed vial filled with argon and used within a couple of days. Water content in solution was measured by Karl Fisher titration, with a Crison Tritomatic 1S. In this case, deposition was performed in a glovebox with a dry nitrogen atmosphere, to control humidity (<10%). During pyrolysis, a dry gas flow was used until 120 °C, before switching to a humid O₂ flow.

Characterization Techniques. Thermogravimetric analysis (TGA) was carried out in a Mettler-Toledo thermobalance, with heating rates of 5 °C/min. The carrier gas was humidified by bubbling a flow of 55 mL/min high-purity gas into a water flask, at 25 °C and 1 atm (3% water).³⁵ To avoid reflux of gaseous species dangerous for the balance, a protective 15 mL/min flow of high-purity synthetic air was used. TG-FTIR coupled experiments were performed by connecting the TG apparatus to an infrared spectrometer by Bruker Alpha II, equipped with a gas cell kept at 200 °C, by means of a 30 cm steel transfer line kept at 200 °C. The spectra were recorded with a spectral resolution of 4 cm⁻¹ and acquisition time of 30 s/spectra. A background spectrum was recorded prior to the experiment. The volatile evolution was plotted choosing a representative wavenumber for each volatile (1779, 2355, and 2740 cm⁻¹, corresponding to propionic acid, CO₂, and acetaldehyde, respectively).

In situ FTIR spectra of the solid residue were recorded at the IR microspectroscopy endstation MIRAS, at the ALBA synchrotron (Spain).³⁶ The end-station was equipped with a Vertex 70 spectrometer, coupled to a visible/IR microscope Hyperion3000, which allows for the focus of the IR radiation on the sample, using a 15× Schwarzschild objective and matching condenser. A Global source was used as IR radiation source, and a nitrogen-cooled MCT detector was used for data acquisition on a 33 μm² sample area. The temperature was controlled using a FTIR600 heating stage (Linkam Scientific Instruments, UK) using CaF₂ windows provided by Crystran Ltd. (UK), which enable the sample to be measured under a continuous gas flow (humid O₂) in transmission mode. Due to the cutoff of the CaF₂ windows, the useful IR range was limited to 4000–1200 cm⁻¹. Spectra were recorded by coadding 10 scans (acquisition time of 10 s) at a spectral resolution of 4 cm⁻¹, while heating the sample between 50 and 500 °C at 10

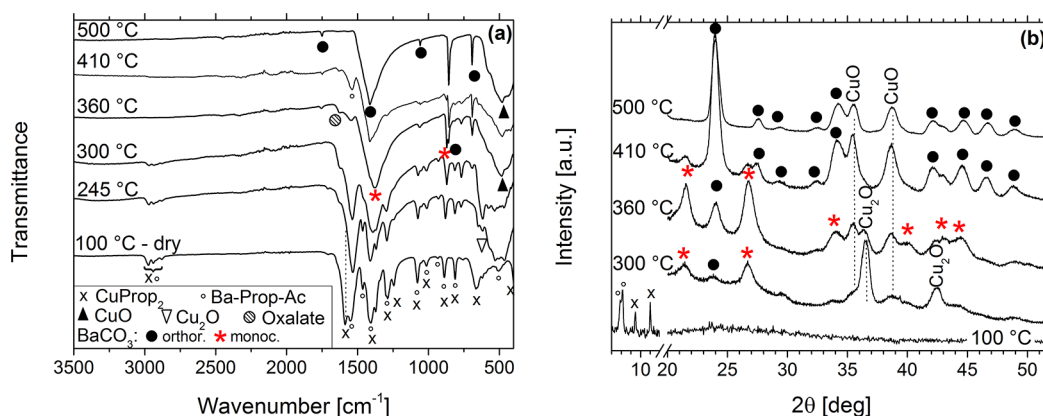


Figure 1. (a) FTIR spectra and (b) corresponding ex situ XRD analysis of the solid residue for $\sim 1 \mu\text{m}$ films of the Cu–Ba binary solution, quenched at given temperatures during decomposition in humid O_2 at $5 \text{ }^\circ\text{C}/\text{min}$. The unexpected monoclinic phase of BaCO_3 appears simultaneously with the copper(II) reduction to $\text{Cu(I)}_2\text{O}$, but it is then converted to the stable orthorhombic phase. FTIR and XRD assignments of the precursors are based on refs 31 and 32.

$^\circ\text{C}/\text{min}$. The raw data was subtracted by the substrate contribution. The absorbance evolution for each species was plotted as a function of temperature, choosing characteristic wavenumbers (1550 cm^{-1} for $\text{C}_2\text{H}_5\text{CO}_2^-$, 1635 cm^{-1} for $\text{C}_2\text{O}_4^{2-}$, 1373 cm^{-1} for CO_3^{2-} ; see contour map in the Supporting Information). More details about setup and data processing are reported in the Supporting Information.

Ex situ X-ray diffraction (XRD) experiments were performed with two diffractometers: The quenched films subjected to thermal treatments were analyzed in grazing incidence with a Bruker-AXS, model A25 D8 Discover, with a $\text{Cu K}\alpha$ anode. The dry precursor films were peeled off the substrates and analyzed with a powder diffractometer to enhance the signal of the salt; the powder diffractometer was a D8 ADVANCE diffractometer from Bruker AXS, with a $\text{Cu K}\alpha$ X-ray beam, operating at a 40 kV voltage and with a 40-mA current.

In situ XRD analysis was performed on the 6-circle diffractometer at the DiffAbs beamline of SOLEIL Synchrotron (France), using 18 keV X-ray photons. The beamline was equipped with an area detector (XPAD, X-ray hybrid pixel area detector) and a furnace (Anton Paar, DHS 1100 model). Specifically, the film sample was placed on the heating plate of the DHS 1100 heater, and a graphite dome was used for confinement. The heater was connected to a gas mixing and control system prepared to achieve different total pressures (P_{tot}) and oxygen partial pressures (P_{O_2}). The system was operated with vacuum pumps and mass flow controllers. An oxygen sensor was used to preset the P_{O_2} value. A fixed grazing incidence geometry was used during in situ experiments, with respective incident and scattering angles of $\omega = 4^\circ$ and $\delta (= 2\theta) \sim 12^\circ$. Using an area detector resulted in the ability to record, in a single image, extended angular regions of the scattered X-ray beam (i.e., portions of an XRD ring), with a range of about 10° in 2θ direction and more than 10° in the ring azimuth direction (as reported in ref 7). By appropriately choosing the 2θ range covered by a single XPAD image, this setup enabled, during in situ annealing, following of the time evolution of the XRD pattern of all the expected phases with an acquisition time of 500 ms/data point. The data was recorded as 2D images for each temperature/time value, which was then mathematically corrected for the geometry of the measurement and converted (azimuthal regrouping) to obtain the intensity versus 2θ curves for each acquisition point. A

significant shift occurs in the 2θ position of the peaks, most probably due to the temperature variation during the experiment, including as well thermal expansion of the whole setup (Figure S3). To represent the evolution of a specific phase, the peak area of a representative peak is plotted versus time (or temperature). More details on data analysis can be found in the Supporting Information.

Ex situ Fourier infrared spectroscopy (FTIR) was carried out with a Bruker Alpha II spectrometer, operating in transmission mode. Scanning transmission electron microscopy (STEM) and electron energy loss spectroscopy (EELS) measurements were performed at the Advanced Microscopy Laboratory in Zaragoza, Spain, with a FEI Titan 60–300 microscope equipped with an X-FEG gun, a CETCOR probe corrector and a Gatan TRIDIEM 866 ERS energy filter operated at 300 kV.

RESULTS

Thermal Decomposition of (Non-Anhydrous) Binary Solutions. In this section, binary combinations of the precursor salts will first be analyzed, and the results will be used to later understand the complex behavior of the ternary precursor solution.

Cu–Ba Binary Solution. Films of the binary solution containing the copper and barium precursors were decomposed in humid O_2 and the solid residue was analyzed ex situ at different temperatures by FTIR and XRD; the results are reported in Figure 1a,b, respectively. Its thermogravimetric curve is shown in Figure 2. The final mass found experimentally, 54%, is in agreement with the theoretical value of 54.0% for the formation of CuO and BaCO_3 .

After deposition, the solvent was not fully removed; this can be seen in the thermogravimetric curve between 50 and $100 \text{ }^\circ\text{C}$. After solvent evaporation, at approximately $100 \text{ }^\circ\text{C}$, from the infrared analysis of this dry film reported in Figure 1a, we note the presence of the intense CuProp_2 band at 1585 cm^{-1} , corresponding to the $\text{C}=\text{O}$ stretching mode, next to the equivalent band for the Ba-Prop-Ac salt which is shifted to 1546 cm^{-1} , higher than the estimated value of $\sim 1530 \text{ cm}^{-1}$.³² As expected, the acetate groups have been fully replaced by propionates in the case of the Cu salt,³¹ because this same FTIR spectra is very similar to that of CuProp_2 . For the barium case, we expect the formation of a mixed Ba-Prop-Ac

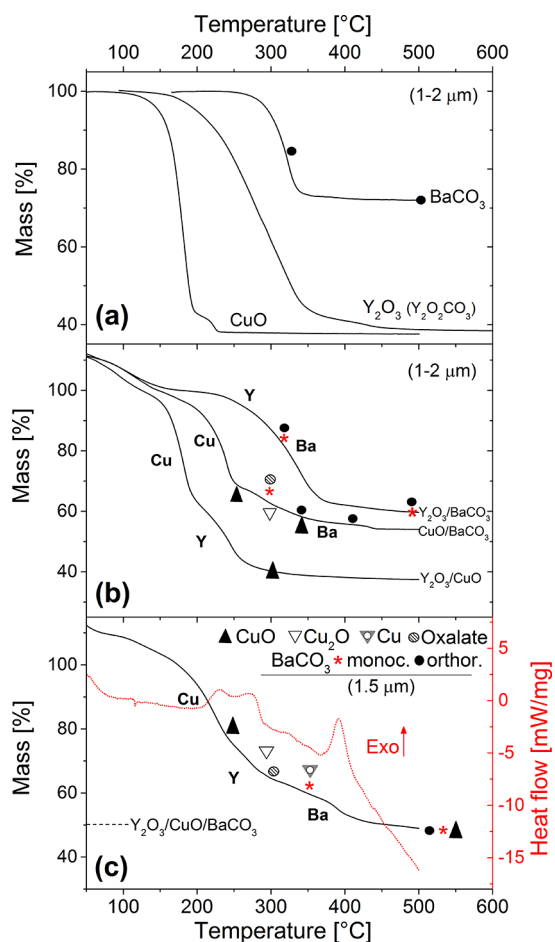


Figure 2. TG curves of (a) single-salt,^{31–33} (b) binary, and (c) ternary solutions of FF-YBCO films decomposed in humid O₂ at 5 °C/min. The symbols on the TG curves indicate when the corresponding phases appear; reduction of copper to Cu(0) only occurs in ternary solutions due to the higher amount of carbon. The presence of the Y precursor does not allow for the monoclinic-to-orthorhombic conversion.

complex.^{32,34} In our multicomponent solution, it is not possible to affirm whether this is true through FTIR, since BaAc₂ most intense bands are hidden by the more abundant CuProp₂. However, the IR bands at 933 cm⁻¹ in Figure 1a could be an indication of the presence of acetate groups. In

addition, the XRD analysis of the powder recovered after drying the solution, reported in Figure 1b, shows two reflections at 8.1 and 7.9°, which are in agreement with the presence of such mixed carboxylate complex. Thus, the starting conditions in the dry film can be considered to be copper propionate and a mixed propionate–acetate salt of barium.

The TG curve of this film, reported in Figure 2b, shows that decomposition starts after solvent evaporation, with two main steps between 150 and 450 °C. By comparison, with the isolated precursors (Figure 2a), it is reasonable to assume that the first mass loss between 150 and 250 °C corresponds to CuProp₂ decomposition to CuO. The FTIR analysis (Figure 1a) at 245 °C confirms the appearance of the CuO IR bands and the disappearance of the CuProp₂ carbonyl band at 1585 cm⁻¹. The heat flow of this first decomposition step is exothermic (Figure S1).

The second mass loss corresponds to the Ba carboxylate decomposition: Between 300 and 360 °C, the FTIR band of an oxalate appears at 1630 cm⁻¹, assigned to BaC₂O₄, showing that the Ba-Prop-Ac salt decomposition is taking place with the expected exothermic signal (Figure S1b). It is followed by copper reduction to Cu₂O, with a maximum intensity at 300 °C, as shown by XRD (Figure 1b). This reduction is surprising, since it is not observed during decomposition of copper propionate alone in an oxidizing atmosphere. As soon as BaC₂O₄ is formed, it is converted to BaCO₃.³² However, unlike the single-salt solution of Ba-Prop-Ac, BaCO₃ does not crystallize into its thermodynamically stable orthorhombic phase but into the monoclinic phase. Thus, at 300 °C, the solid residue mainly consists of a mixture of monoclinic BaCO₃ and cuprous oxide. Above 350 °C, Cu₂O is reoxidized to CuO (see XRD in Figure 1b), and the monoclinic phase is reconverted to the stable orthorhombic structure. At 500 °C, this phase and CuO are the final products observed by XRD.

Cu–Y and Y–Ba Binary Solutions. In the Cu–Y binary solution, replacement of acetates by propionates takes place as well, as shown by the FTIR spectrum of the dry film (Figure 3a). This is again expected from the behavior of the separate salts.^{31,33} Additionally, the presence of yttrium propionate and copper propionate is confirmed by XRD in Figure S1a. In the TG curve of Figure 2, the final mass lies at 37%, very close to the theoretical value of 37.4% for the formation of CuO and Y₂O₃.

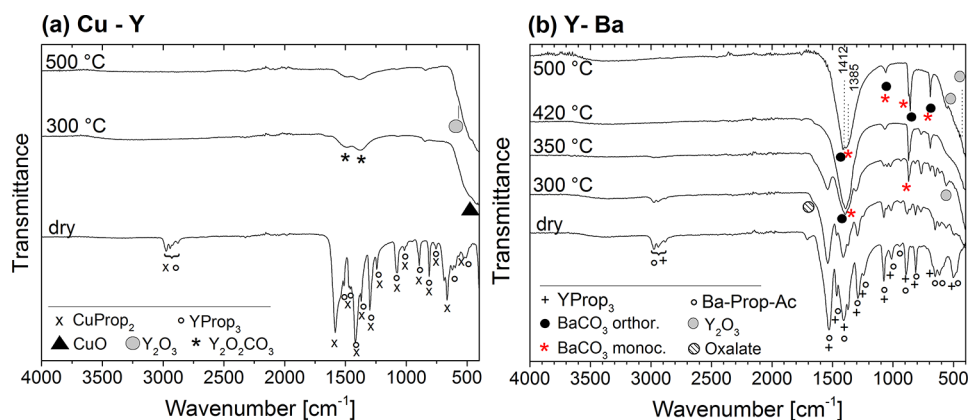


Figure 3. FTIR spectra of the solid residue of quenched samples of (a) Cu–Y solutions and (b) Y–Ba solutions for thick films (>1 μm). FTIR assignments of the precursors follow refs 31, 32, and 33.

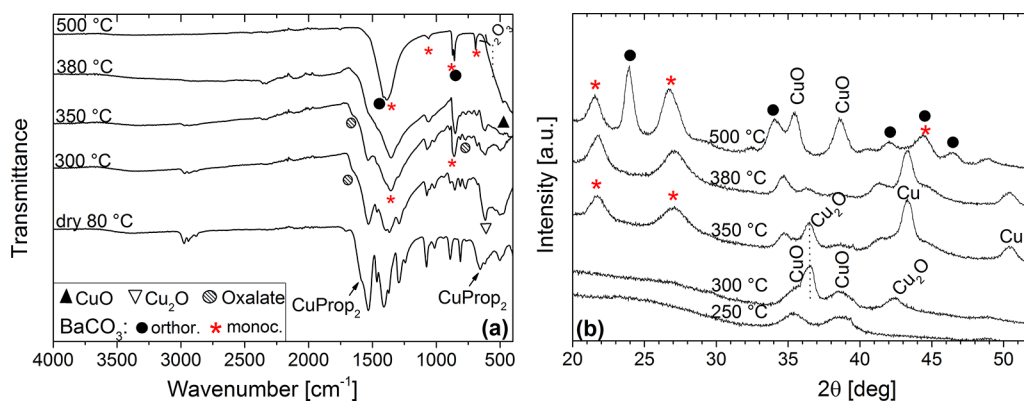


Figure 4. (a) FTIR and (b) XRD evolution of the solid residue of quenched samples during decomposition in humid O_2 at $5^\circ/\text{min}$ of $\sim 1.5 \mu\text{m}$ film of non-anhydrous ternary solution. The reduction of Cu(II) is due to the carbon carried by the other salts. Note the formation of $BaCO_3$ monoclinic in the presence of $Cu(0)/Cu_2O$.

In the same TG curve, two steps can be clearly distinguished: the first one between 100 and 200 $^\circ\text{C}$, and the second step between 200 and 400 $^\circ\text{C}$, after which the mass is stable. In the first stage, decomposition of $CuProp_2$ takes place. Indeed, at 300 $^\circ\text{C}$, CuO is detected by FTIR and XRD analysis (Figures 3a and S1a), and the heat evolved is slightly endothermic (Figure S1) as expected in humid O_2 at this temperature.³¹ Note that in Figure 2b, decomposition of the copper precursor in Cu–Y films takes place roughly 50 $^\circ\text{C}$ earlier than in the Cu–Ba film. Since the films have similar thickness, the barium precursor in Cu–Ba films is probably slowing down the decomposition due to its higher stability.³² In the second stage, $YProp_3$ decomposition occurs, and the DTA signal is exothermic (Figure S1b). Therefore, no copper reduction is observed at 300 $^\circ\text{C}$, probably because the whole organic fraction has decomposed before this temperature. This fact suggests that CuO reduction in the Cu–Ba solution is due to the C/CO released during the barium salt decomposition. The final products consist of Y_2O_3 and CuO , both identified by XRD (Figure S1b). Just like the case of yttrium propionate alone,^{18,33} residual yttrium oxycarbonate, $Y_2O_2CO_3$, is detected only by FTIR (asterisks in Figure 3a), in agreement with the fact that it decomposes above 600 $^\circ\text{C}$.¹⁸

In the binary Y–Ba solutions, acetates are again replaced by propionates. In fact, the dry film analyzed by infrared spectroscopy consists of $YProp_3$ (“+” in Figure 3b) and $BaProp\text{-}Ac$ (empty circles in Figure 3b). The most intense IR band at 1529 cm^{-1} comprises the C=O stretching vibrations of both the yttrium and barium precursors.^{32,33} The TG curve reported in Figure 2 shows one main mass loss step, with the final mass stable at 59.6%, quite well in agreement with the expected 59.4% for Y_2O_3 and $BaCO_3$ formation. Quenched films at different temperatures during decomposition were analyzed by FTIR (Figure 3b). The analysis of the solid residue shows that at 300 $^\circ\text{C}$ the $BaCO_3$ is starting to crystallize. At 500 $^\circ\text{C}$, the final product consists of monoclinic and orthorhombic $BaCO_3$ and Y_2O_3 . In contrast with the Cu–Ba film, the monoclinic phase still coexists with the orthorhombic equilibrium phase at this temperature.

Thermal Decomposition of (Non-Anhydrous) Ternary Solutions. *TG-IR and Ex Situ FTIR and XRD Analysis.* The study of the binary solutions is crucial to unravel the different decomposition steps hidden in the complex behavior of the three-component solution. The TG analysis of ternary solutions is reported in Figure 2c. Despite the fact that it is

hard to separate the initial dehydration from the decomposition, the final mass percentage found experimentally, 49%, is in reasonable agreement with the expected value of 50.3% for the formation of Y_2O_3 , CuO , and $BaCO_3$ (considering $Ba_7Prop_8Ac_6$ as precursor). Note that the 100% mass line has been set with the help of the mass derivative (dTG) analysis.

Just like the binary solutions, the first stage consists of solvent evaporation, between 50 and 150 $^\circ\text{C}$. This is reasonable because, especially for drop-cast films, not all solvent can be removed during the drying stage. Water and propionic acid absorptions (between 3000 and 4000 cm^{-1} and at $\sim 1708 \text{ cm}^{-1}$) are still visible by FTIR in Figure 4a, at 80 $^\circ\text{C}$. This step is also observed in other TG curves of the same solution (see Figure 5).

After solvent evaporation, the propionate reflections are detected (FTIR in Figure 4a), with the C=O stretching band of $CuProp_2$ visible at $\sim 1583 \text{ cm}^{-1}$. Those of the yttrium and barium salts overlap at $\sim 1530 \text{ cm}^{-1}$.

In the second stage (150–250 $^\circ\text{C}$), from the infrared and X-ray analysis of quenched samples during decomposition, it is evident that $CuProp_2$ decomposition between 150 and 250 $^\circ\text{C}$ is the first decomposition to take place; this is confirmed by the fact that by 250 $^\circ\text{C}$ the CuO XRD reflections appear (Figure 4b). The volatiles expected from the $CuProp_2$ oxidation in humid O_2 are propionic acid (below 200 $^\circ\text{C}$), CO_2 , and CH_3CHO (above 200 $^\circ\text{C}$) coming from the hydrolysis and oxidative decomposition of the propionate unit. The TG-IR analysis of a ternary film (Figure 5) confirms that these gaseous species are indeed detected in this stage, between 150 and 250 $^\circ\text{C}$. In particular, after 200 $^\circ\text{C}$, the heat flow signal is exothermic, as expected due to the oxidation reactions^{32,33} responsible for CO_2 and acetaldehyde formation.

Between 250 and 350 $^\circ\text{C}$, while decomposition of the other salts takes place, CuO is first reduced to Cu_2O at $\sim 300 \text{ }^\circ\text{C}$, and then to metallic copper, Cu , at 350 $^\circ\text{C}$ (Figure 4). This suggests that the residual carbon or CO released from the other two salts pushes toward the reduction of CuO upon CO_2 release, according to the following reaction: $CuO + CO \rightarrow Cu + CO_2$. This is followed by a series of CO_2 peaks in the EGA analysis. Although CO_2 is being released by the decomposition of the yttrium and barium salts alone in oxygen,^{18,29,32,33} part of this CO_2 is actually ascribed in the literature to the oxidation of the released CO/C. In turn, CO comes from the decomposition of the intermediate barium oxalate^{32,37} and from the oxidation path of yttrium propionate to acetalde-

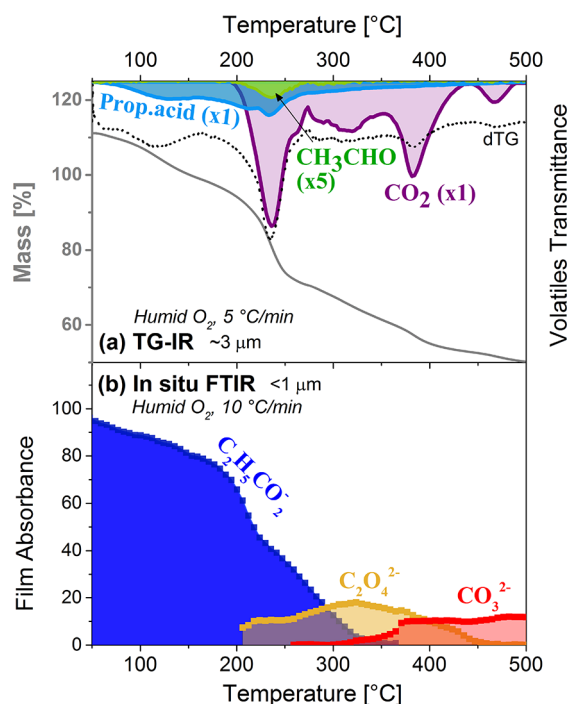


Figure 5. (a) TG curve, its time derivative (dTG, dotted line), and TG-IR analysis of a drop-cast 3 μm film of ternary solution, measured during pyrolysis to 500 $^{\circ}\text{C}$ in humid O₂ at 5 $^{\circ}\text{C}/\text{min}$. Compared to films of the single-salt solutions, the main decomposition volatile is CO₂ and the decomposition process is shifted to higher temperatures. (b) In situ IR analysis of the evolution of the solid residue of spin-coated films, performed at the ALBA synchrotron facility in humid O₂ and 10 $^{\circ}\text{C}/\text{min}$.

hyde.³³ The carbon comes from the disproportionation of CO to C and CO₂.³⁷ In fact, as film thickness increases, gas transport slows down, and CO oxidation is delayed, favoring its disproportionation. This explains the detection of residual carbon at 500 $^{\circ}\text{C}$ for both Y and Ba propionates,^{32,33} especially in powders. In the ternary solution of this work, since not just one but two carboxylate salts are added with respect to a Cu–Ba binary solution, reduction is pushed all the way to Cu due to the higher availability of carbon to produce CO₂. Simultaneously, with copper oxide reduction to Cu₂O and to Cu,

BaCO₃ starts to crystallize in the monoclinic phase between 300 and 350 $^{\circ}\text{C}$. No signal from the YProp₃ decomposition is clearly detected, even by FTIR analysis, because its absorptions are hidden by those of Cu and Ba species, which are present in greater amounts.

In the last stage, between 350 and 450 $^{\circ}\text{C}$, copper is reoxidized to Cu(II), and some orthorhombic BaCO₃ phase appears. The heat flow is exothermic (Figure 2c), as expected from the single-salt behavior of the barium precursor.³² The final product consists of a mixture of orthorhombic and monoclinic BaCO₃, along with CuO, while Y₂O₃ is probably not observed by XRD due to its small grain size. The ternary solution seems to follow the behavior of a Ba–Y solution, where the orthorhombic phase is not fully recovered at 500 $^{\circ}\text{C}$. In both binary and ternary solutions, the FTIR analysis of this specific solution is alone sufficient to distinguish the contribution of the orthorhombic BaCO₃ (peaks at ~ 1416 and 856 cm^{-1}) from the monoclinic BaCO₃ (peaks at ~ 1382 and 872 cm^{-1}), as demonstrated by complementing the FTIR with the XRD analysis in Figure 4.

In Situ FTIR Spectroscopy. It was also possible to follow in situ the infrared evolution of the solid residue of a thin (<1 μm) ternary film decomposed in similar conditions to the previous samples, by FTIR. Measurements were performed at the infrared microspectroscopy beamline MIRAS of the ALBA synchrotron facility. The information acquired, reported in Figure 5b, is limited to a small IR range ($4000\text{--}1200\text{ cm}^{-1}$, see the “Methods” section), but it is complementary to the information already provided by the quenched samples of Figure 4. The main processes that can be identified are in good agreement with the analysis derived from the volatiles and the mass loss information in Figure 5a. This is not surprising, even though thinner films are expected to decompose at lower temperature, because in this case the effect of the film thickness is compensated by that of a higher heating rate (10 instead of 5 $^{\circ}\text{C}/\text{min}$), which shifts all thermally activated processes to higher temperatures.³⁸

Between 50 and 150 $^{\circ}\text{C}$, we observe the presence of the propionate salts. The gradual decrease observed in film absorbance can be attributed to a background signal decrease due to propionic acid evaporation and water. This is in agreement with the TG analysis of Figure 5a, where mostly the

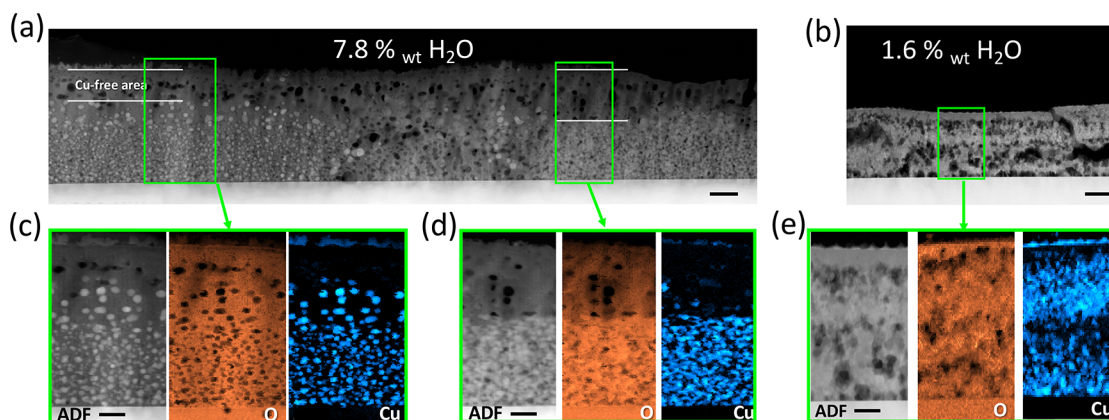


Figure 6. (a, b) High-angle annular dark field (HAADF)-STEM images of spin-coated samples pyrolyzed to 500 $^{\circ}\text{C}$, with different water content in solution (wt %). The higher the water percentage, the lower the porosity of the layer. Bar scale = 200 nm. (c–e) O K and Cu L edge EELS elemental maps of selected areas of images shown in panels (a) and (b), respectively, showing residual metallic copper in the case of the sample shown in panel (a). Bar scale = 100 nm.

solvent (propionic acid absorption) is detected around 100 °C. However, in the thin film of Figure 5b, it is hard to distinguish the end of evaporation with the beginning of CuProp₂ decomposition, which could have already started between 100 and 150 °C.

Between 150 and 350 °C, due to the decomposition of the propionates, the intensity of the carboxylate vibrations decreases significantly until it disappears. Meanwhile, the IR absorptions in the 1600–1700 cm⁻¹ range increase between 300 and 350 °C, which can be attributed to the formation of the barium oxalate unstable intermediate. Finally, between 350 and 500 °C, we observe an increase of the CO₃²⁻ absorption band, which we can attribute to the decomposition of the barium species to form BaCO₃, mostly in the monoclinic phase.

Effects of Additional Parameters on the Pyrolysis Process. In all the previous sections, the pyrolysis of the precursor solution was analyzed under non-anhydrous conditions. However, we observed that the water percentage in solution, attributed to the hygroscopic nature of precursors and solvents used, has a crucial influence on the final film properties; in particular, a detrimental effect on BaCO₃ decomposition is observed when the water amount is high. Some of the causes can be connected to the fact that water affects both the crystalline phases and the microstructure of the film formed during pyrolysis. Since it is crucial to ensure reproducibility throughout the entire CSD processing of YBCO films, this section will focus on some of these effects in more detail.

Microstructure of the Pyrolyzed Film: Effect of Water. In terms of film microstructure, we observed by STEM analysis (Figure 6), that a high water content in solution is responsible for a more compact film after pyrolysis (Figure 6a). In particular, going from 1.6% (Figure 6b) to 7.8% water content in the initial solution (Figure 6a), the overall porosity of the processed layer decreases after pyrolysis, and very compact areas are visible throughout the layer. If we consider that the water content can change the rheological properties (i.e., viscosity, wettability) and the coordination of the metal salts of the precursor solution, then it is also likely that these properties in turn affect the way the layer rearranges under the physical stress caused by evaporation and decomposition.

This compactness may hinder gas transport and, in particular, slow down oxygen transport through the layer. This helps us explain, for example, why metallic copper is found in these compact regions of the bottom parts of the film (see the EELS elemental maps in Figure 6c). In regions that are closer to areas with higher porosity, as in Figure 6d, the EELS maps show a more homogeneous oxygen signal, indicating the presence of more CuO and less Cu nanoparticles. However, a copper-free area is found toward the film surface in both Figure 6c,d, suggesting that some Cu precursor has sublimated in films prepared from solutions with high water content. Conversely, in areas of greater layer porosity like in Figure 6b,e, the EELS maps show that the copper and oxygen signals overlap, indicating that no significant Cu(0) is detected. In these spin-coated films of Figure 6 (<1 μm), Cu(0) survives until 500 °C, while in the quenched thicker films analyzed by XRD in Figure 4, Cu(0) is reoxidized to CuO before 500 °C. Since thicker films prepared by drop-casting are more likely to crack during decomposition, this subsequently higher porosity can favor copper oxidation, explaining why Cu(0) is not observed by XRD at 500 °C in

Figure 4. Finally, the metallic copper intermediate has a tendency to coarsen, thus explaining the presence of larger (>10 nm) CuO grain size observed after pyrolysis of non-anhydrous solutions (not shown).

BaCO₃ Formation and Decomposition: Effect of Water. The other crystalline phase affected by the presence of water is the monoclinic BaCO₃ phase. This is formed after pyrolysis only when there is high water content in the initial solution (>2%wt), which is the case in Figure 6a (XRD analysis in Figure S4). Conversely, anhydrous conditions during solution preparation and deposition, such as in Figure 6d, are associated with the presence of the orthorhombic phase after pyrolysis (Figure S4). Thus, we observed that irreproducibility issues in the final YBCO film microstructure and properties may arise because different BaCO₃ decomposition behaviors take place depending on the BaCO₃ crystalline phase (monoclinic, M, or orthorhombic, O) obtained after pyrolysis. These results are shown in Figure 7. In these experiments, the BaCO₃

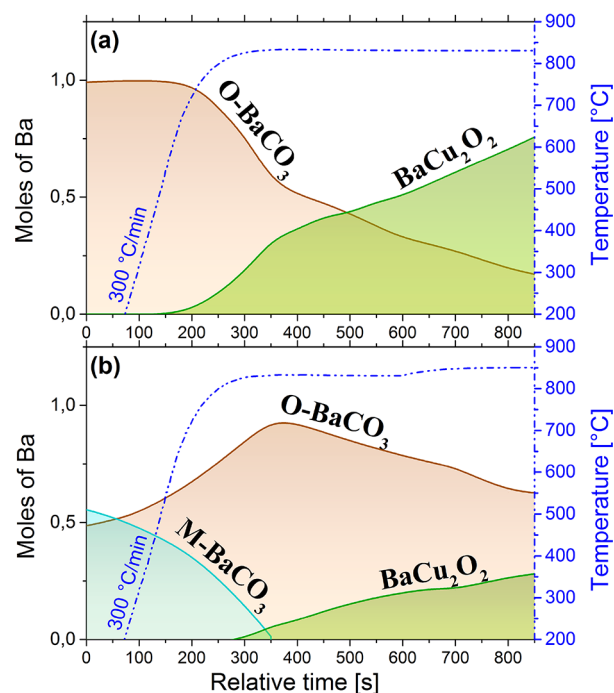


Figure 7. Evolution of the Ba-containing phases of two pyrolyzed ternary films (~700 nm at 500 °C) with different initial ratios of monoclinic (M) and orthorhombic (O) BaCO₃, obtained by in situ XRD. The number of barium moles is normalized to 1. The amount of O-BCO₃ and BaCu₂O₂ is obtained from their peak areas whereas that of M-BCO₃ is obtained by subtraction from unity (see the Supporting Information). Conditions of the in situ XRD experiments: P_{O₂} ~ 10⁻⁵ bar, dry atmosphere and heating ramp of 300 °C/min.

decomposition was followed by in situ synchrotron XRD analysis during the heating ramp of the pyrolyzed samples toward the YBCO film growth. In particular, Figure 7 compares the decomposition of two pyrolyzed films containing different M/O ratios (increasing from panel a to b in Figure 7), treated in a dry atmosphere at P_{O₂} = 10⁻⁵ bar and low gas flow. In this route, the oxides and carbonates are heated up in a region of the phase diagram below the YBCO instability line,^{39,40} to promote the BaCO₃ decomposition via the following reaction path:⁷ BaCO₃ + Cu₂O → BaCu₂O₂ + CO₂. This is followed by a fast oxygen pressure increase to

reach the region above the YBCO instability line. Upon this P_{O_2} increase, the system is able to form a transient liquid which enables the ultrafast YBCO growth, via the TLAG route introduced by Soler et al.⁷ Therefore, the decomposition of the carbonate is crucial to achieve subsequent YBCO growth.

Figure 7 reveals two essential aspects: First, M-BaCO₃ is converted to the stable O-BaCO₃ phase prior to decomposition, and second, the initial presence of M-BaCO₃ is associated with a delay of the carbonate decomposition, revealed by both the slower diminution of the O-BaCO₃ content and the slower growth rate of the BaCu₂O₂ product. By looking at the phase evolution, the delay in the formation of O-BaCO₃ can be attributed to the time needed for the reconversion of the monoclinic phase to the equilibrium phase (O-BaCO₃). The subsequent O-BaCO₃ decomposition may be slower because the delay in its formation from the monoclinic phase favors phase coarsening. Furthermore, the existence of M-BaCO₃ is correlated with non-anhydrous conditions which, as described in the previous section, result in greater film compactness that renders CO₂ out-diffusion more difficult. Nevertheless, it is important to mention that the exact time and decomposition temperatures for BaCO₃ reported in Figure 7 are likely to be affected by the specific experimental conditions in which decomposition is carried out (gas flow, film thickness, total pressure, and partial oxygen pressure). Independent of these parameters, avoiding the formation of M-BaCO₃ stands out as a critical objective in order to shorten processing time and increase film performances.

The connections between the presence of water and the formation of the monoclinic phase is not yet clear. Some clues can be found in the way that water was found to affect the crystal structure and thermal history of the precursors used, both BaProp₂ and Ba-Prop-Ac. In non-anhydrous solutions of only the barium salt, they retain crystallization water in their structures (Ba₇Prop₈Ac₆·4H₂O,³² Ba₇Prop₁₀Ac₄·5H₂O,³⁴ and BaProp₂·H₂O)⁴¹ up to relatively high temperature. By differential scanning calorimetry (DSC) analysis, it was observed in ref 32 that upon dehydration these salts undergo melting and recrystallization events (endothermic DSC peaks in Figure S5) prior to decomposition which are not all reversible. This indicates that the initial structures are not the equilibrium ones, since they cannot be recovered by simply reversing the temperature.

We observed that the DSC peak associated with the first phase change (Figure S5, between 200 and 300 °C) and thus the original phase could be recovered by redissolving the barium salt obtained after the phase change (280 °C) in non-anhydrous methanol and propionic acid, where coordination with water could again occur. This suggests that the phase change may be attributable to water in solution.

Interestingly, these transformations alone are not enough to promote formation of M-BaCO₃, since this phase is not observed after pyrolysis of the single-component solution of any barium precursors (BaProp₂, BaAc₂, and mixed propionate-acetate barium salts); it is only observed when another salt (of yttrium or copper, or both) is present along with the propionate-based barium precursor. Thus, the presence of yttrium or copper seed species may influence the recrystallization phases of the barium species, especially if melting events are involved.³²

We should therefore expect that barium salts without these phase changes during the pyrolysis range are more likely to

yield O-BaCO₃ at 500 °C. For example, BaAc₂ does not show phase changes (note the straight heat flow signal in Figure S6) during most of the pyrolysis range, between 50 and 450 °C. Additionally, BaAc₂ is anhydrous already at relatively low temperatures, above 30–40 °C,⁴² and the anhydrous form is crystalline⁴³ and stable in atmospheric air. In fact, a ternary mixture containing BaAc₂ instead of BaProp₂ or Ba-Prop-Ac was pyrolyzed to 500 °C in non-anhydrous conditions, and it predominantly formed O-BaCO₃ (see Figure S6). Although not much literature data could be found regarding the crystalline intermediates formed during pyrolysis, this is in agreement with the behavior of other solutions consisting of acetates.^{44,45}

Finally, the presence of these unexpected phases might be independently promoted by other causes too. For example, the initial degree of crystallinity (or the more amorphous nature) of the precursor salts after deposition could also affect the final crystalline phases and grain size.

Overall, the data provided in this section suggest that the presence of water in our solution can be detrimental to layer properties, because we identified experimental conditions in which it causes the formation of non-equilibrium intermediate phases before YBCO crystallization, with the consequence of delaying BaCO₃ decomposition.

DISCUSSION

The analysis of the ternary solution of CSD fluorine-free precursors of YBCO films used in this work showed that its behavior during the pyrolysis thermal treatment of pyrolysis is more complex than the behavior expected from the simple sum of its components. Still, previous knowledge about decomposition of the single-component precursor solutions is fundamental to understand the decomposition of the binary and ternary solutions. In particular, the decomposition order in both binary and ternary solutions seems to generally follow the temperatures for the isolated metal propionate salts in films: Copper propionate is the first to decompose, while the barium precursor salt is the last. Nevertheless, other effects arise as a consequence of the interaction of the three salts that were not possible to foresee from the study of the single-salt solutions alone.

One of these unexpected outcomes is the copper reduction leading to intermediate non-equilibrium phases, even in an oxidizing atmosphere. Even though copper reduction to Cu(I) is easily promoted during decomposition of copper propionate films in inert atmospheres, it is never observed during pyrolysis in humid O₂.³¹ In the ternary system, the release of C or CO from other salts is able to reduce the copper oxide to Cu₂O and even to metallic copper. The other unexpected outcome is the formation of the non-equilibrium monoclinic phase of BaCO₃, which is never observed from decomposition of single barium acetate, barium propionate, or Ba-Prop-Ac films in any atmosphere, where the orthorhombic phase is always the product recovered in non-anhydrous conditions.^{32,34} The fact that the presence of yttrium or copper species is necessary to promote the formation of the monoclinic phase, indicates that complex relationships are at play, whose origin could be related to the presence of unstable barium precursor crystalline structures. Alternatively, if gas transport is hindered by a very low layer porosity, then the local atmosphere can also change, which in turn could be responsible for the phase in which BaCO₃ crystallization occurs.

The presence of these two phases is not desirable because they are accompanied by a different microstructure and because an extra step is then required to reconvert them to the intermediates from which YBCO can grow. Specifically, the reduced copper needs to be reoxidized to the equilibrium CuO phase, and this process depends on the ability to promote gas transport through the layer. Similarly, M-BaCO₃ needs to be reconverted to O-BaCO₃ before its decomposition can begin. It is upon the reaction of O-BaCO₃ with CuO that the Ba–Cu–O transient liquid forms, giving rise to the ultrafast growth of YBCO from TLAG-CSD, as discussed in ref 7 from in situ synchrotron XRD experiments.

Although for our specific solution and furnace setup working in anhydrous conditions was found to favor the crystallization of the equilibrium O-BaCO₃ and CuO phase, anhydrous conditions are not always the preferred cost-effective choice. Thus, other control parameters for these CSD solutions should be sought that can be used to promote the existence of certain phases over others. For example, the resulting microstructure could be tuned by changing the solution's rheological properties, or the slow gas exchange could be compensated for with the use of a higher gas flux and the right furnace design, which can enable a faster local atmosphere renewal.

Actually, the fact that formation of metallic copper and M-BaCO₃ had also been observed at 360 °C with other ternary solutions of different precursors such as lactates⁴⁶ is an indication that, all in all, these phases may have common and consistent origins. This origin can be linked to the high amount of carbon generated by the decomposition of the metal–organic precursors, the degree of porosity of the layer, and the competing precursor crystalline structures promoted by water. Therefore, the metal–organic salts chosen, the water content of the solution, the rheological properties of the solution, and the gas flow will all determine the phases obtained.

Even though this issue will require further investigation, it is clear that many parameters besides water content are involved during pyrolysis of these CSD ternary solutions and that thermal analysis coupled to analytical and structural techniques are crucial to disentangle them.

CONCLUSIONS

In conclusion, we have shown the need to study the decomposition of the precursor solution and the evolution of the intermediate phases in the growth of YBCO films from TLAG-CSD. We demonstrated that the ternary solution based on propionate fluorine-free precursors of YBCO decomposes following the theoretical oxidation order of its isolated component salts. Surprisingly, new effects also arise that are not observed in the single-component solutions: Cu(II) is reduced to Cu(0) even in humid O₂, while a non-equilibrium BaCO₃ phase, the monoclinic one, is formed, which can be detrimental to the carbonate decomposition step. While the presence of copper reduction could be ascribed to carbon or CO coming from decomposition of the other salts, further investigation is necessary to disclose the reasons for the monoclinic phase with certainty. The results suggest that the two phases might be interlinked and that their origin may ultimately be connected to the chemistry of the precursors and to the ability to promote gas transport during the decomposition step. In our case, the monoclinic BaCO₃ and metallic copper are avoided after pyrolysis by adopting

rigorously anhydrous conditions during preparation and deposition of the propionate solution.

ASSOCIATED CONTENT

Supporting Information

The Supporting Information is available free of charge at <https://pubs.acs.org/doi/10.1021/acs.jpcc.0c03859>.

Additional thermal analysis figures and details on in situ FTIR and XRD experiments (PDF)

AUTHOR INFORMATION

Corresponding Author

Silvia Rasi – *Universitat de Girona, Campus Montilivi, E17003 Girona, Spain; Institut de Ciència de Materials de Barcelona, ICMA B – CSIC, Campus UAB, E-08193 Barcelona, Spain;* orcid.org/0000-0003-4935-3918; Email: silvia.rasi@udg.edu

Authors

Laia Soler – *Institut de Ciència de Materials de Barcelona, ICMA B – CSIC, Campus UAB, E-08193 Barcelona, Spain*

Julia Jareño – *Institut de Ciència de Materials de Barcelona, ICMA B – CSIC, Campus UAB, E-08193 Barcelona, Spain*

Juri Banchewski – *Institut de Ciència de Materials de Barcelona, ICMA B – CSIC, Campus UAB, E-08193 Barcelona, Spain*

Roger Guzman – *Institut de Ciència de Materials de Barcelona, ICMA B – CSIC, Campus UAB, E-08193 Barcelona, Spain*

Cristian Mocuta – *Synchrotron SOLEIL, 91192 Gif-sur-Yvette, France;* orcid.org/0000-0001-5540-449X

Martin Kreuzer – *Synchrotron Alba, 08290 Barcelona, Spain;* orcid.org/0000-0002-7305-5016

Susagna Ricart – *Institut de Ciència de Materials de Barcelona, ICMA B – CSIC, Campus UAB, E-08193 Barcelona, Spain;* orcid.org/0000-0003-4196-2081

Pere Roura-Grabulosa – *Universitat de Girona, Campus Montilivi, E17003 Girona, Spain*

Jordi Farjas – *Universitat de Girona, Campus Montilivi, E17003 Girona, Spain*

Xavier Obradors – *Institut de Ciència de Materials de Barcelona, ICMA B – CSIC, Campus UAB, E-08193 Barcelona, Spain;* orcid.org/0000-0003-4592-7718

Teresa Puig – *Institut de Ciència de Materials de Barcelona, ICMA B – CSIC, Campus UAB, E-08193 Barcelona, Spain*

Complete contact information is available at: <https://pubs.acs.org/doi/10.1021/acs.jpcc.0c03859>

Notes

The authors declare no competing financial interest.

ACKNOWLEDGMENTS

This work was funded by Ministerio de Ciencia, Innovación y Universidades (RTI2018-095853-B-C21 and RTI2018-095853-B-C22) cofinanced by the European Regional Development Fund, and the EU Ultrasupertape project (ERC ADG-2014-669504). We also acknowledge the Center of Excellence Severo Ochoa (SEV-2015-0496), the Generalitat de Catalunya (2017-SGR-1519) and the COST-action NANOCOHYBRI (CA16218). In situ FTIR experiments were performed at the MIRAS beamline of the ALBA Synchrotron with the collaboration of ALBA staff. We also thank the DiffAbs beamline at SOLEIL Synchrotron facility

and the beamline staff support for the in situ XRD experiments. We thank the ICMAB, INA-Zaragoza and UdG scientific services and technical staff for the support on the experiments. S.R. thanks the Universitat de Girona (UdG) for the IFuG grant. L.S. and J.J. also acknowledge their FPU-MINECO PhD grant.

REFERENCES

- (1) Obradors, X.; Puig, T. Coated conductors for power applications: materials challenges. *Supercond. Sci. Technol.* **2014**, *27*, 044003.
- (2) Palmer, X.; Pop, C.; Eloussifi, H.; Villarejo, B.; Roura, P.; Farjas, J.; Calleja, A.; Palau, A.; Obradors, X.; Puig, T.; Ricart, S. Solution design for low-fluorine trifluoroacetate route to $\text{YBa}_2\text{Cu}_3\text{O}_7$ films. *Supercond. Sci. Technol.* **2016**, *29*, 024002.
- (3) Ciontea, L.; Angrisani, A.; Celentano, G.; Petrisor, T., jr.; Rufoloni, A.; Vannozzi, A.; Augieri, A.; Galuzzi, V.; Mancini, A.; Petrisor, T. Metal propionate synthesis of epitaxial $\text{YBa}_2\text{Cu}_3\text{O}_{7-x}$ films. *Journal of Physics: Conference Series* **2008**, *97*, 012302.
- (4) Maeda, H.; Yanagisawa, Y. Recent developments in high-temperature superconducting magnet technology (Review). *IEEE Trans. Appl. Supercond.* **2014**, *24*, 1–12.
- (5) Obradors, X.; Puig, T.; Gibert, M.; Queralto, A.; Zabaleta, J.; Mestres, N. Chemical solution route to self-assembled epitaxial oxide nanostructures. *Chem. Soc. Rev.* **2014**, *43*, 2200–2225.
- (6) Schneller, T.; Waser, R.; Kosec, M.; Payne, D., Eds. *Chemical Solution Deposition of Functional Oxide Thin Films*; Springer, 2013.
- (7) Soler, L.; Jareño, J.; Banchewski, J.; Rasi, S.; Chamorro, N.; Guzman, R.; Yáñez, R.; Mocuta, C.; Ricart, S.; Farjas, J. Ultrafast transient liquid assisted growth of high current density superconducting films. *Nat. Commun.* **2020**, *11*, 344.
- (8) Puig, T.; González, J. C.; Pomar, A.; Mestres, N.; Castaño, O.; Coll, M.; Gázquez, J.; Sandiumenge, F.; Piñol, S.; Obradors, X. The influence of growth conditions on the microstructure and critical currents of TFA-MOD $\text{YBa}_2\text{Cu}_3\text{O}_7$ films. *Supercond. Sci. Technol.* **2005**, *18*, 1141–1150.
- (9) Araki, T.; Hirabayashi, I. Review of a chemical approach to $\text{YBa}_2\text{Cu}_3\text{O}_{7-x}$ coated superconductors - metalorganic deposition using trifluoroacetates. *Supercond. Sci. Technol.* **2003**, *16*, R71–R94.
- (10) Obradors, X.; Puig, T.; Ricart, S.; Coll, M.; Gázquez, J.; Palau, A.; Granados, X. Growth, nanostructure and vortex pinning in superconducting $\text{YBa}_2\text{Cu}_3\text{O}_7$ thin films based on trifluoroacetate solutions. *Supercond. Sci. Technol.* **2012**, *25*, 123001.
- (11) Piperno, L.; Rasi, S.; De Santis, S.; Masi, A.; Santoni, A.; Mancini, A.; Angrisani, A.; Pinto, V.; Farjas, J.; Sotgiu, G.; Celentano, G.; et al. Elucidation of the decomposition reactions of low-fluorine $\text{YBa}_2\text{Cu}_3\text{O}_{7-x}$ precursors during film pyrolysis. *J. Anal. Appl. Pyrolysis* **2020**, *148*, 104777.
- (12) Vermeir, P.; Feys, J.; Schaubroeck, J.; Verbeke, K.; Lommens, P.; Van Driessche, I. V. Influence of sintering conditions in the preparation of acetate-based fluorine-free CSD YBCO films using a direct sintering method. *Mater. Res. Bull.* **2012**, *47*, 4376–4382.
- (13) Nasui, M.; Petrisor, T.; Mos, R. B.; Gabor, M. S.; Mesaros, A.; Goga, F.; Ciontea, L.; Petrisor, T. Fluorine-free propionate route for the chemical solution deposition of $\text{YBa}_2\text{Cu}_3\text{O}_{7-x}$ superconducting films. *Ceram. Int.* **2015**, *41*, 4416–4421.
- (14) Jasim, S. E.; Jusoh, M. A.; Hafiz, M.; Jose, R. Fabrication of Superconducting YBCO Nanoparticles by Electrospinning. *Procedia Eng.* **2016**, *148*, 243–248.
- (15) Zuo, J. L.; Zhao, Y.; Wu, W.; Chu, J. Y.; Zhang, Z. W.; Hong, Z. Y.; Jin, Z. J. Intermediate Phase Evolution in YBCO Superconducting Film Fabricated by Fluorine Free MOD Method. *Wuji Cailiao Xuebao* **2018**, *33*, 773–778.
- (16) Mu, J.; Perlmutter, D. Thermal decomposition of carbonates, carboxylates, oxalates, acetates, formates and hydroxides. *Thermochim. Acta* **1981**, *49*, 207–218.
- (17) Kalsi, P. C.; Bassi, P.; Khajuria, C. M. Kinetics of the isothermal decomposition of Cu(II). *Thermochim. Acta* **1980**, *41*, 265–268.
- (18) Grivel, J. Thermal decomposition of yttrium(III) propionate and butyrate. *J. Anal. Appl. Pyrolysis* **2013**, *101*, 185–192.
- (19) Grivel, J. Thermal decomposition of lutetium propionate. *J. Anal. Appl. Pyrolysis* **2010**, *89*, 250–254.
- (20) Grivel, J. Thermal decomposition of $\text{Ln}(\text{C}_2\text{H}_3\text{CO}_2)_3 \cdot \text{H}_2\text{O}$ ($\text{Ln} = \text{Ho, Er, Tm}$ and Yb). *J. Therm. Anal. Calorim.* **2012**, *109*, 81–88.
- (21) Roura, P.; Farjas, J.; Ricart, S.; Akkouch, M.; Guzman, R.; Arbiol, J.; Puig, T.; Calleja, A.; Peña-Rodríguez, O.; Garriga, M.; et al. Synthesis of nanocrystalline ceria thin films by low-temperature thermal decomposition of Ce-propionate. *Thin Solid Films* **2012**, *520*, 1949–1953.
- (22) Roura, P.; Farjas, J.; Eloussifi, H.; Carreras, L.; Ricart, S.; Puig, T.; Obradors, X. Thermal analysis of metal organic precursors for functional oxide preparation: Thin films versus powders. *Thermochim. Acta* **2015**, *601*, 1–8.
- (23) Sánchez-Rodríguez, D.; Farjas, J.; Roura, P. The critical conditions for thermal explosion in a system heated at a constant rate. *Combust. Flame* **2017**, *186*, 211–219.
- (24) Akanni, M. S.; Okoh, E. K.; Burrows, H. D.; Ellis, H. A. The thermal behaviour of divalent and higher valent metal soaps: a review. *Thermochim. Acta* **1992**, *208*, 1–41.
- (25) Akanni, M. S.; Ajayi, O. B.; Lambi, J. N. Pyrolytic decomposition of some even chain length copper(II) carboxylates. *J. Therm. Anal.* **1986**, *31*, 131–143.
- (26) Akanni, M. S.; Burrows, H.; Begun, P. B. Product analysis, reaction mechanism and kinetics of the thermal decomposition of some even chain-length mercury(II) carboxylates. *Thermochim. Acta* **1984**, *81*, 45–58.
- (27) Szczęsny, R.; Szlyk, E. Thermal decomposition of some silver (I) carboxylates under nitrogen atmosphere. *J. Therm. Anal. Calorim.* **2013**, *111*, 1325–1330.
- (28) Martynova, I. A.; Tymbarenko, D. M.; Kuz'mina, N. P. Yttrium tris-propionate monohydrate: Synthesis, crystal structure, and thermal stability. *Russ. J. Coord. Chem.* **2014**, *40*, 565–570.
- (29) Nasui, M.; Bogatan, C.; Ciontea, L.; Petrisor, T. Synthesis, crystal structure modeling and thermal decomposition of yttrium propionate ($\text{Y}_2(\text{CH}_3\text{CH}_2\text{COO})_6 \cdot \text{H}_2\text{O}$) $\cdot 3.5\text{H}_2\text{O}$. *J. Anal. Appl. Pyrolysis* **2012**, *97*, 88–93.
- (30) Nasui, M.; Petrisor, T., Jr.; Mos, R. B.; Mesaros, A.; Varga, R. A.; Vasile, B. S.; Ristoiu, T.; Ciontea, L.; Petrisor, T. Synthesis, crystal structure and thermal decomposition kinetics of yttrium propionate. *J. Anal. Appl. Pyrolysis* **2014**, *106*, 92–98.
- (31) Rasi, S.; Silveri, F.; Ricart, S.; Obradors, X.; Puig, T.; Roura-Grabulosa, P.; Farjas, J. Thermal decomposition of CuProp_2 : In-situ analysis of film and powder pyrolysis. *J. Anal. Appl. Pyrolysis* **2019**, *140*, 312–320.
- (32) Rasi, S.; Ricart, S.; Obradors, X.; Puig, T.; Roura-Grabulosa, P.; Farjas, J. Radical and oxydative pathways in the pyrolysis of a barium propionate-acetate salt. *J. Anal. Appl. Pyrolysis* **2019**, *141*, 104640.
- (33) Rasi, S.; Ricart, S.; Obradors, X.; Puig, T.; Roura, P.; Farjas, J. Thermal decomposition of yttrium propionate: film and powder. *J. Anal. Appl. Pyrolysis* **2018**, *133*, 225–233.
- (34) Mos, R. B.; Nasui, M.; Petrisor, T., Jr.; Gabor, M. S.; Varga, R.; Ciontea, L.; Petrisor, T. Synthesis, crystal structure and thermal decomposition study of a new barium acetato-propionate complex. *J. Anal. Appl. Pyrolysis* **2011**, *92*, 445–449.
- (35) Bridgeman, O. C.; Aldrich, E. W. Vapor Pressure Tables for Water. *J. Heat Transfer* **1964**, *86*, 279.
- (36) Yousef, I.; Ribó, L.; Crisol, A.; Sics, I.; Ellis, G.; Ducic, T.; Kreuzer, M.; Benseny-Cases, N.; Quispe, M.; Dumas, P.; et al. MIRAS: The Infrared Synchrotron Radiation Beamline at ALBA. *Synchrotron Radiation News* **2017**, *30*, 4–6.
- (37) Verdonk, A. H.; Broersma, A. Thermal decomposition of barium oxalate hemihydrate $\text{BaC}_2\text{O}_4 \cdot 0.5\text{H}_2\text{O}$. *Thermochim. Acta* **1973**, *6*, 95–110.
- (38) Farjas, J.; Roura, P. Exact analytical solution for the Kissinger equation: Determination of the peak temperature and general properties of thermally activated transformations. *Thermochim. Acta* **2014**, *598*, 51–58.

(39) MacManus-Driscoll, J. L.; Bravman, J. C.; Beyers, R. B. Phase equilibria in the Y-Ba-Cu-O system and melt processing of Ag clad $Y_1Ba_2Cu_3O_{7-x}$ tapes at reduced oxygen partial pressures. *Phys. C* **1995**, *241*, 401–413.

(40) Lindemer, T.; Washburn, F.; MacDougall, C. S. Study of phase behavior in the $YBa_2Cu_3O_{7-x}$ - $BaCuO_{2+y}$ -CuO-Ag system. *Phys. C* **1992**, *196*, 390–398.

(41) Gobert-Ranchoux, E.; Charbonnier, F. Comportement thermique des propionates hydrates de calcium, strontium et baryum. *J. Therm. Anal.* **1977**, *12*, 33–42.

(42) Walker, J.; Fyffe, W. A. The hydrates and the solubility of barium acetate. *J. Chem. Soc., Trans.* **1903**, *83*, 173–182.

(43) Gautier-Luneau, I.; Mosset, A. Crystal structure of anhydrous barium acetate. *J. Solid State Chem.* **1988**, *73*, 473–479.

(44) Vermeir, P.; Cardinael, I.; Schaubroeck, J.; Verbeken, K.; Backer, M.; Lommens, P.; Knaepen, W.; D'haen, J.; De Buysser, K.; Van Driessche, I. Elucidation of the mechanism in fluorine-free prepared $YBa_2Cu_3O_{7-\delta}$ coatings. *Inorg. Chem.* **2010**, *49*, 4471–4477.

(45) Thuy, T. T.; Hoste, S.; Herman, G. G.; De Buysser, K.; Lommens, P.; Feys, J.; Vandeput, D.; Van Driessche, I. Sol-gel chemistry of an aqueous precursor solution for YBCO thin films. *J. Sol-Gel Sci. Technol.* **2009**, *52*, 124–133.

(46) Lei, L.; Zhao, G.; Zhao, J.; Xu, H. Water-vapor-controlled reaction for fabrication of YBCO films by fluorine-free sol-gel process. *IEEE Trans. Appl. Supercond.* **2010**, *20*, 2286–2293.